Optimized Temporary Frequency Support for Wind Power Plants Considering Expanded Operational Region of Wind Turbines

Zhengyang Hu, *Member*, *IEEE*, Bingtuan Gao, *Senior Member*, *IEEE*, Zhao Xu, *Senior Member*, *IEEE*, and Sufan Jiang, *Member*, *IEEE*

***Abstract*—Wind power plants (WPPs) are increasingly mandated to provide temporary frequency support to power systems during contingencies involving significant power shortages. However, the frequency support capabilities of WPPs under derated operations remain insufficiently investigated, highlighting the potential for further improvement of the frequency nadir. This paper proposes a bi-level optimized temporary frequency support (OTFS) strategy for a WPP. The implementation of the OTFS strategy is collaboratively accomplished by individual wind turbine (WT) controllers and the central WPP controller. First, to exploit the frequency support capability of WTs, the stable operational region of WTs is expanded by developing a novel dynamic power control approach in WT controllers. This approach synergizes the WTs' temporary frequency support with the secondary frequency control of synchronous generators, enabling WTs to release more kinetic energy without causing a secondary frequency drop. Second, a model predictive control strategy is developed for the WPP controller. This strategy ensures that multiple WTs operating within the expanded stable region are coordinated to minimize the magnitude of the frequency drop through efficient kinetic energy utilization. Finally, comprehensive case studies are conducted on a real-time simulation platform to validate the effectiveness of the proposed strategy.**

***Index Terms*—Active power control model predictive control, optimized temporary frequency support, wind power plant, wind turbine.**

I. Introduction

WIND energy has experienced rapid development over the past few years, emerging as one of the most effective solutions for mitigating energy shortages and advancing carbon neutrality goals [1]–[3]. Integrating wind power into power systems significantly reduces dependency on fossil fuels. In order to facilitate wind power consumption, the maximum power point tracking (MPPT) control is widely adopted. However, high share wind power with MPPT control, which is unresponsive to frequency variations or deviations, poses challenges to maintaining power system frequency stability and security [4]–[6]. For example, the bipolar blocking in Jinping-Suzhou ± 800 kV high-voltage direct current (HVDC) transmission in China caused a frequency fall of 0.41 Hz on 19 September 2015 [7]. The blackout in Great Britain on 9 August 2019 was caused by the frequency drop resulting from the power shortage of over 1000 MW, resulting in approximately 1.1 million customers being without power for about 30 minutes [8]. To enhance the frequency stability and security of power systems, many countries have mandated the participation of wind power plants (WPPs) in frequency regulation [9]–[11].

Research on the frequency support strategies of WPPs can be mainly categorized into two types: MPPT-based control [12]–[32] and deloading-based control [33]–[37]. Overall, a significant difference in adopting these two methods for WTs lies in the operational regions of WTs. Under MPPT-based control, WTs decelerate to operate on the left side of the maximum power point (MPP) when supporting a system frequency drop by releasing kinetic energy [20]. In contrast, under deloading-based control, WTs are typically required to operate in the region to the right of the MPPT curve, even during frequency support [37].

The WPP with the MPPT control scheme can provide temporary frequency support [18], with a temporal scale that matches the inertial response and primary frequency regulation of synchronous generators (SGs). There are three categories of the MPPT-based temporary frequency support strategy: frequency-based inertial control [12]–[16], stepwise inertial control (SIC) [17]–[23], and optimized frequency support [28]–[32]. Frequency-based inertial control typically involves an additional control loop to improve the frequency nadir (FN) based on the measured rate of change of frequency (RoCoF) [12] or the combination of the frequency deviation and RoCoF [13], [14]. However, the selection of appropriate control parameters in diverse operational scenarios presents a considerable challenge. To mitigate this challenge, the utiliza-

Manuscript received February 22, 2024; revised May 7, 2024; accepted July 4, 2024. Date of online publication January 10, 2025; date of current version January 15, 2025. This work was supported by the National Key R&D Program of China under Grant 2021YFB2400500.

Z. Y. Hu is with the School of Electrical Engineering, Southeast University, Nanjing 210096, China, and also with the Department of Electrical and Electronic Engineering, The Hong Kong Polytechnic University, Hong Kong SAR, China.

B. T. Gao (corresponding author, email: gaobingtuan@seu.edu.cn) is with the School of Electrical Engineering, Southeast University, Nanjing 210096, China.

Z. Xu is with the Department of Electrical and Electronic Engineering, The Hong Kong Polytechnic University, Hong Kong SAR, China.

S. F. Jiang is with the Department of Electrical Engineering and Computer Science, The University of Tennessee, Knoxville, TN 37996 USA.

DOI: 10.17775/CSEEJPES.2024.01340

tion of an adaptive inertial parameter is proposed in [15], while [16] suggests employing model predictive control (MPC) for tuning the droop controller gain in wind turbines (WTs).

Nevertheless, ongoing measurement of the frequency and RoCoF will lead to a delayed response and diminished frequency support effectiveness [17]. Accordingly, the SIC approaches are developed to improve the frequency support effects of WTs without frequency measurements [19], [20]. Upon the detection of a frequency event, the SIC promptly increases the active power output of WTs and maintains this elevated production level for a predetermined period [21]. In pursuit of a minimized frequency drop, the MPC method is utilized in WPPs to achieve an optimal active power value and support duration of SIC [22]. Most research on SIC focuses on the improvements of FN by tuning control parameters including the magnitude of support power values and the length of support times [17], [23]. Yet, it is important to note that the efficacy of SIC strategies in improving FN is inherently constrained by their fixed support patterns, which typically adopt a square waveform or its modified variants.

Furthermore, the issue of the secondary frequency drop (SFD) resulting from the termination of temporary frequency support by WTs remains unresolved. Mitigating SFD typically entails either reducing the strength of frequency support or prolonging the rotor speed recovery time of WTs [22], [24]–[27]. A diminished frequency support strength does not optimally suppress frequency drops. At the same time, prolonged rotor speed recovery can compromise the overall frequency support in the event of sudden wind speed fluctuations, leading to an exacerbated SFD [17].

Given the inadequacies in traditional frequency support strategies, there has been increasing concern regarding the need for optimized frequency support. A temporary frequency support control strategy, enhanced by optimizing control parameters, is proposed in [28], but this approach inherently relies on a transfer function combining primary frequency regulation with droop control. An optimal inertial control for the WPP employing a triangle wave trajectory of active power support is proposed in [29]. However, such fixed-pattern approaches to active power support fail to fully exploit the potential for improving frequency regulation (FN). To overcome the limitation of fixed-pattern strategies, a transient frequency regulation strategy for WTs is proposed to optimize the active power support trajectory, aiming for economic efficiency while ensuring frequency security as a constraint [30]. However, the differences in operational states among WTs and the active power support capability of WTs are neglected. Another type of optimized frequency support strategy utilizes data-driven methods, enabling a more authentic portrayal of the output characteristics of WPPs and the frequency characteristics of power systems [31], [32]. Nevertheless, the limited amount of data, along with insufficient data refinement, impedes the development and application of these methods.

The WPP with the deloading-based control scheme can provide sustained frequency support from the suboptimal power point on the right side of the MPP. Rotor speed control and pitch angle regulation constitute the primary methods for attaining power reservation [33]. To provide fast and sustained frequency support from the suboptimal power point, MPC-based primary frequency regulation is proposed in [34]. To maintain the small-signal stability of WTs, they should avoid operating on the left side of the MPP [35]. Consequently, in a sustained frequency support strategy utilizing deloading-based control, WTs generally operate on the right side of the MPP. This approach effectively mitigates the issue of SFD, a primary concern in MPPT-based frequency support [34]–[37].

To promote the stability of the power system frequency, WPPs ought to track the power instructions dispatched by the system operator [38], [39], and the scheduling instructions are generally less than the predicted maximum power. Therefore, WPPs need to curtail the active power to track the instructions, and WTs will accordingly operate on the right side of the MPP. Under this scheme, the releasable kinetic energy of WTs is constrained compared with the aforementioned MPPT-based frequency support, which is not suitable for contingency scenarios that demand strong frequency support. Thus, it is necessary to study a novel control strategy for WTs to provide temporary frequency support from the right region to the left.

As introduced in the review, substantial advancements have been realized in the frequency support of the WPP with both MPPT-based and deloading-based control. Nevertheless, there remain areas where further investigation is needed to bridge existing knowledge gaps. 1) Incomplete consideration of the operational region of WT is adopted in research, which splits the left and right regions of the MPPT curve. 2) Most studies design transfer function-based frequency support strategies to imitate the frequency response characteristics of SGs, or design a fixed operating trajectory for WTs to support the frequency, but there is still a lack of techniques for selecting optimal active power support trajectories for WTs under various operational states to maximize the improvement of FN.

In this study, an optimized temporary frequency support (OTFS) strategy for WPP is proposed, which not only suppresses the frequency overshoot caused by the delay in the primary frequency response of SGs but also utilizes the secondary frequency control (SFC) of SGs to provide energy for the recovery of WTs rotor speed, offering a novel approach to frequency regulation in WPPs. The main contributions can be summarized as follows.

1) A temporary power point tracking (TPPT) strategy is proposed for each WT to enhance its temporary frequency support capability and to synergize this support with the SFC of SGs, enabling WTs to operate to the left of the MPPT curve without inducing the SFD.

2) An MPC-based OTFS strategy is developed for the WPP to optimize online the trajectories for all the WTs' active power support, aiming to minimize the magnitude of the system frequency drop through rational utilization of the limited kinetic energy of each WT.

The remainder of the paper is structured as follows. Section II presents the bi-level control framework. In Section III, the TPPT strategy for individual WTs is proposed. Section IV provides a detailed design of the MPC-based OTFS strategy for the WPP. Section V presents and discusses the results of the case studies. Finally, Section VI offers the conclusions.

II. Bi-Level Control Framework

A bi-level control framework is developed to facilitate coordination between the dynamic power control strategy in WTs' controllers and the MPC strategy in WPP's controller to collectively implement an OTFS, as shown in Fig. 1. The WT level should follow the power command from the WPP level and maintain the stability of rotor speed after the temporary frequency support. In contrast, trajectory optimization and control instruction decisions are managed at the WPP level. This framework is fit for both double-fed induction generator (DFIG)-based WT and permanent magnetic synchronous generator (PMSG)-based WT due to their similar electromechanical transient characteristics of frequency response. The DFIG-based WT is taken as an example in Fig. 1.

In the WT level, WTs should follow the active power command $P_{\mathrm{wcmd}i,j}$ in the steady state. If the frequency drop event occurs, the support power instructions of individual WTs $\Delta P_{\mathrm{OTFS}i,j}$ will be dispatched from the WPP's controller. WTs will release the stored kinetic energy to participate in the frequency regulation. In previous studies, if the WTs reduce the rotor speed to the left region of the MPPT curve after the frequency support, WTs will return to the MPPT mode according to a pre-defined operating trajectory. To exploit the frequency support capability of WTs and avoid the SFD caused by the WTs' withdrawal from the temporary frequency support, a TPPT strategy is proposed. Thus the WTs can stably operate in the left region. In the TPPT control strategy, the measured rotor speeds $\omega_{\mathrm{w}i,j}$ of individual WTs are used to generate the power reference $P_{\mathrm{TPPT}i,j}$. The power system requires strong temporary frequency support from the WPP in contingency scenarios to avoid excessive frequency drop, while the strong support requires the WTs to slow down to the left side of the MPPT curve to release more kinetic energy. Since the SFC will eventually compensate for the frequency deviation, the WPP will not return to the normal operation status until the SFC works. The stability analysis of the WTs operating in different areas and the TPPT strategy are detailed in Section III.

According to the schedule of the system operator, the active power reference of the WPP P_{WPPref} is decided and delivered to the WPP's controller. When the frequency event occurs, the WPP level predicts the state variable. It optimizes the WPP's active power support trajectory according to the current power system state, load disturbances, and the wind speed $v_{\mathrm{w}i,j}$ and rotor speed $\omega_{\mathrm{w}i,j}$ of individual WTs. The predictive model includes the frequency response characteristics of the system and the operation state of each WT. The control variables of the model are the support power instruction $\Delta P_{\mathrm{OTFS}i,j}$ of each WT. The receding horizon optimization objectives are to minimize the magnitude of frequency drop and suppress the excessive actions of WTs. Considering the limited kinetic energy of WTs, the incremental power and support energy consumption are described as constraints. By dynamically solving the optimization problem, the support power instructions of individual WTs $\Delta P_{\mathrm{OTFS}i,j}$ are updated at each sampling time. Further information is provided in Section IV.

III. TPPT Strategy for Individual WTs

A. Aerodynamics Model and Drive Train Model of WT

The mechanical power captured by the WT from the wind energy, P_{wm}, is shown [18]

$$\begin{cases} P_{\mathrm{wm}} = 0.5\rho\pi R_{\mathrm{w}}^2 C_{\mathrm{P}}(\lambda,\beta)v_{\mathrm{w}}^3 \\ \lambda = \omega_{\mathrm{w}} R_{\mathrm{w}}/v_{\mathrm{w}} \end{cases} \tag{1}$$

where ρ, R_{w}, v_{w}, C_{P}, β, λ, and ω_{w} are the air density, rotor radius, wind speed, power coefficient, pitch angle, tip-speed ratio, and the rotor speed of the WT respectively.

This study assumes a rigidly coupled drive train, employing a single-mass model as referenced in [38]. The drive train model per unit (pu) can be expressed by

$$\begin{cases} \dot{\omega}_{\mathrm{w}} = (T_{\mathrm{wm}} - T_{\mathrm{we}})/2H_{\mathrm{w}} \\ T_{\mathrm{wm}} = P_{\mathrm{wm}}/\omega_{\mathrm{w}} \\ T_{\mathrm{we}} = P_{\mathrm{we}}/\omega_{\mathrm{g}} \end{cases} \tag{2}$$

where T_{wm} and T_{we} are the mechanical and electromagnetic torque of the WT, H_{w} is the inertia constant of the WT, P_{we} is the electromagnetic power of the WT, and ω_{g} is the generator rotor speed. The per unit value of ω_{w} and ω_{g} are the same.

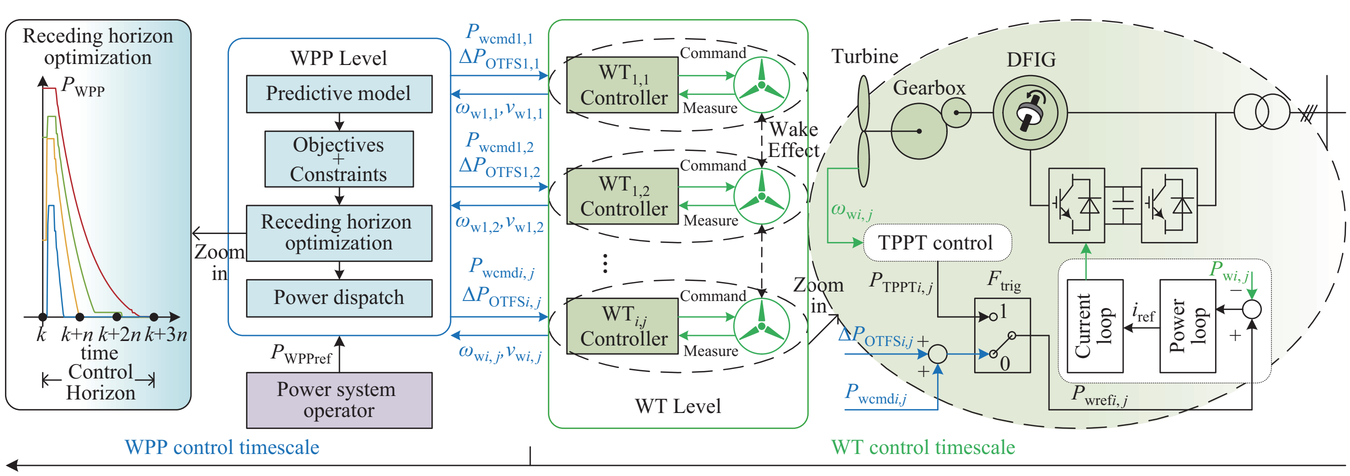

Fig. 1. Bi-level control framework of the proposed OTFS strategy.

B. WT's Operational Region Analysis

The operational region of a WT is divided into two parts. The region on the right side of the MPPT curve is called the stable region, and the left side is called the temporary region, as shown in Fig. 2.

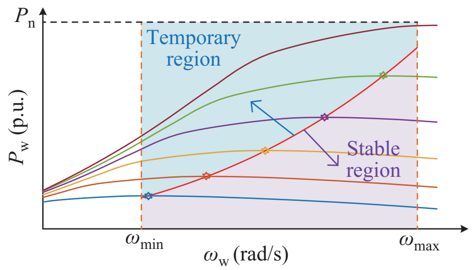

Fig. 2. Operational region of a WT.

The following is the analysis of the WT's small-signal stability in the temporary region. The main operational disturbance for each WT is wind fluctuation. According to (1) and (2), the stability analysis of WT in the temporary region is shown as:

$$\begin{cases} v_w \uparrow \Rightarrow T_{wm} \uparrow \Rightarrow \omega_w \uparrow \Rightarrow C_p \uparrow \Rightarrow T_{wm} \uparrow\uparrow \Rightarrow \omega_w \uparrow\uparrow \\ v_w \downarrow \Rightarrow T_{wm} \downarrow \Rightarrow \omega_w \downarrow \Rightarrow C_p \downarrow \Rightarrow T_{wm} \downarrow\downarrow \Rightarrow \omega_w \downarrow\downarrow \end{cases} \tag{3}$$

If the wind speed v_w decreases, the mechanical torque T_{wm} will decrease. Since the electromagnetic torque remains unchanged, the rotor speed ω_w will also decrease. According to the aerodynamic characteristics of WTs, the power coefficient will decrease with the decreasing of ω_w, and then the T_{wm} and ω_w will further decrease.

It can be obtained that the variation of the wind speed will cause increasing changes in the rotor speed of the WT in the temporary region. However, the electromagnetic torque can be revised to offset the impact of mechanical torque changes, avoiding the over-deceleration of the rotor speed. Thus, the active power control strategy of WTs can be modified to ensure the rotor speed stability within a temporary region.

C. Temporary Power Point Tracking Control of WTs

In order to avoid the SFD after the temporary frequency support, the operational region can be expanded. Since it is unstable for WTs to operate on the left side of the MPPT curve, as analyzed in Section II-C, auxiliary control should be adopted to compensate for wind or electromagnetic torque disturbances.

According to (3), wind speed variation will lead to the rotor speed instability. This conclusion is derived under the assumption that the electromagnetic torque is constant. If the active power reference of the WT can be modified with rotor speed, similar to the MPPT method, the asymptotic stability of WT might be achieved. Therefore, a temporary power point tracking (TPPT) strategy is proposed, as shown in Fig. 3. Here, ω_{max} and ω_{min} are the upper and lower limits of the rotor speed of the WT. ω_{tem} indicates the rotor speed at the time of withdrawing from temporary frequency support, and P_n is the nominal power of the WT.

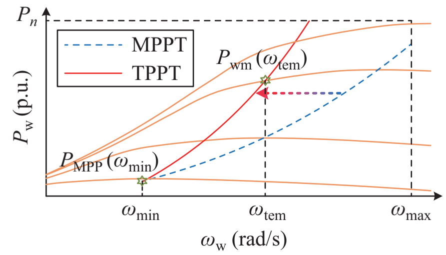

Fig. 3. The proposed TPPT curve of WT.

The yellow line is the power-speed performance curve corresponding to (1). The blue curve is the traditional MPPT curve, expressed as:

$$\begin{cases} P_{MPP} = k_{opt}\omega_w^3 \\ k_{opt} = 0.5\rho\pi R_w^5 C_{Popt}/\lambda_{opt}^3 \end{cases} \tag{4}$$

where C_{Popt} and λ_{opt} are the optimal power coefficient and the optimal tip-speed ratio of the WT. Referenced to the MPPT curve, a TPPT curve is designed as:

$$P_{TPPT} = k_{tem}(\omega_w + x)^3 \tag{5}$$

To ensure the designed TPPT curve can make the WT meet the asymptotic stability requirement, the feasible range of P_{TPPT} should be analyzed, so that the parameters k_{tem} and x can be determined. Based on the Lyapunov theorem, the energy function is established as:

$$V = (\omega_w - \omega_{tem})^2 \tag{6}$$

V is a positive definite function. V equals 0 only when ω_w equals ω_{tem}. V is greater than 0 as long as ω_w is not equal to ω_{tem}. According to the Lyapunov theorem, if V satisfies that $\dot{V}$ is less than 0 when ω_w is not equal to ω_{tem}, the asymptotic stability of the system can be guaranteed. The generalized energy is continuously consumed and stabilized in the dynamic process. The derivatives of (6) is deduced as:

$$\dot{V} = 2(\omega_w - \omega_{tem})\dot{\omega}_w \tag{7}$$

Since the mechanical response time is much slower than the electromagnetic one, the electromagnetic torque control (inner loop) can be assumed to be well controlled when focusing on the active power control (outer loop) [40]. Thus, the T_{we} is equal to the electromagnetic torque reference, and the P_{we} is equal to the P_{wref}. Once the TPPT control is activated, the P_{wref} is equal to the P_{TPPT}, and the derivatives of ω_w can be obtained

$$\dot{\omega}_w = \frac{1}{2H_w}(T_{wm} - T_{we}) = \frac{1}{2H_w\omega_w}(P_{wm} - P_{TPPT}) \tag{8}$$

Then, (7) can be rewritten as:

$$\dot{V} = (\omega_w - \omega_{tem})(P_{wm} - P_{TPPT})/H_w\omega_w \tag{9}$$

It is obtained from (9) that $\dot{V} < 0$ can be satisfied when $(\omega_w - \omega_{tem})(P_{wm} - P_{TPPT})$ is less than 0. Thus, the P_{TPPT} should satisfy the following equation

$$\begin{cases} P_{TPPT} < P_{wm}, & \omega_w < \omega_{tem} \\ P_{TPPT} > P_{wm}, & \omega_w > \omega_{tem} \end{cases} \tag{10}$$

In this situation, it can be obtained that (11) is always satisfied.

$$\dot{V} < 0, \ \omega_{\mathrm{w}} \neq \omega_{\mathrm{tem}} \tag{11}$$

If the P_{TPPT} satisfies (10), the Lyapunov asymptotic stability of the WT is always satisfied during the dynamic process. Then, to ensure the control stability, let the TPPT curve pass through point $P_{\mathrm{MPP}}(\omega_{\min})$ and the current working point $P_{\mathrm{wm}}(\omega_{\mathrm{tem}})$ shown in Fig. 3. Substituting into (5), we get

$$\begin{aligned} k_{\mathrm{tem}} &= P_{\mathrm{wm}}(\omega_{\mathrm{tem}}) \times \left[\sqrt[3]{P_{\mathrm{MPP}}(\omega_{\min})/P_{\mathrm{wm}}(\omega_{\mathrm{tem}})} - 1 \right]^3 \\ &\quad /(\omega_{\min} - \omega_{\mathrm{tem}})^3 \\ x &= (\omega_{\min} - \omega_{\mathrm{tem}}) / \left[\sqrt[3]{P_{\mathrm{MPP}}(\omega_{\min})/P_{\mathrm{wm}}(\omega_{\mathrm{tem}})} - 1 \right] \\ &\quad - \omega_{\mathrm{tem}} \end{aligned} \tag{12}$$

The TPPT control diagram is shown in Fig. 4.

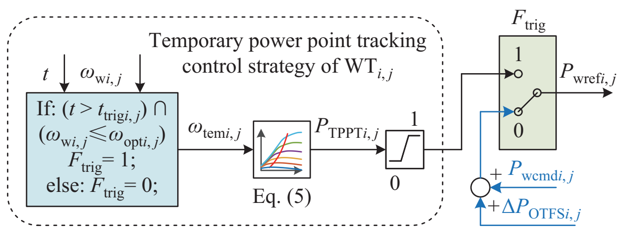

Fig. 4. TPPT control strategy of $WT_{i,j}$.

In Fig. 4, $t_{\mathrm{trig}i,j}$ is the time duration of temporary frequency support, and $F_{\mathrm{trig}i,j}$ is the flag for triggering. If the WT operates in the temporary region when it withdraws from the temporary frequency support, the $F_{\mathrm{trig}i,j}$ will be set to 1 and the TPPT control loop will be triggered. Consequently, the TPPT strategy will not be concurrently activated with the frequency support strategy at the WPP level. The TPPT strategy serves as a critical link between temporary frequency support provided by WTs and secondary frequency regulation of synchronous generators. Although similar to the MPPT curve as a cubic function of WTs' rotor speed, the TPPT curve is uniquely computed for each WT based on its specific operating conditions. This approach ensures that the WTs can stabilize their rotor speeds as effectively as possible in the left region of the MPPT curve post temporary frequency support.

It is noted that although TPPT will operate the WTs at a low-efficiency point, it is of short duration and has a limited impact on the annual generation and revenue of the WPP.

D. Rotor Speed Recovery Strategy

The objective of the TPPT strategy is to temporarily operate the WT in the temporary region. At the same time, it is necessary to return to the stable region after the triggering of the SFC. Consequently, a WT's rotor speed recovery process considering the SFC of the thermal power generation unit is still required. The SFC model for thermal power generation units is illustrated in Fig. 5, and the specific control parameter is referenced in [41] and [42].

In Fig. 5, B is the frequency bias stated in p.u./0.1 Hz, ΔP_{tie} is the tie-line power flow variation, f_{dbd} is the frequency

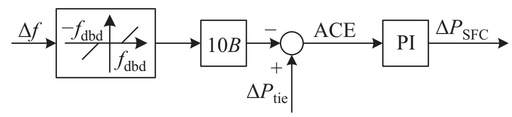

Fig. 5. SFC model.

error tolerance dead-band, ACE is the area control error of frequency, ΔP_{SFC} is the incremental power of SFC. The SFC of thermal power generation units requires the involvement of the grid dispatch center to issue instructions, typically responding at the minute level after an event occurs [43]. In this study, the activation of the SFC is set to begin 1 minute after the fault occurrence.

After a few seconds of initiating the SFC, the WT restores its operation from the temporary power point to the steady-state working point. Considering the extensive research on the speed recovery of WTs following frequency support exit, this study adopts the recovery strategy proposed in [20], with an added step for transitioning from the MPP to the derated power point, as illustrated in Fig. 6.

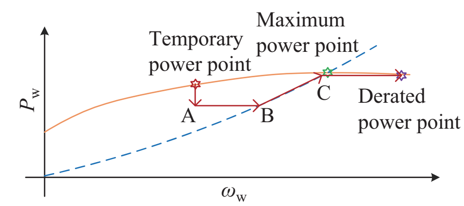

Fig. 6. Power-rotor speed trajectory during the recovery process.

The rotor speed recovery trajectory for individual WTs initiates from the temporary power point. It follows a path through points A, B, and C until it finally converges at the derated power point. Thus, the design of the control strategy for the WT level is accomplished.

IV. MPC-BASED OTFS STRATEGY FOR WPP

The primary objective of the frequency support strategy is to optimize the active power trajectories of WTs to enhance the FN during significant frequency drop events. This problem can be formulated as a receding horizon optimization within a finite time domain. The risk of the SFD can be neglected in the optimization of the TPPT strategy. The detailed design steps of the proposed MPC-based OTFS strategy for the WPP are as follows.

A. System Frequency Response Model

The system frequency response (SFR) following a disturbance can be forecasted using a simplified low-order SFR model. By disregarding elements with minor time constants, the predictive model and associated optimization problem are significantly simplified. The small-signal SFR model in pu can be expressed as [44]

$$\begin{cases} 2H_{\mathrm{s}}\Delta\dot{f} + (D_{\mathrm{s}} - K_{\mathrm{m}}F_{\mathrm{H}}/R)\Delta f = K_{\mathrm{m}}\Delta X_1 - \Delta P_{\mathrm{L}} \\ T_{\mathrm{R}}\Delta\dot{X}_1 + \Delta X_1 = (1 - F_{\mathrm{H}})\Delta f/R \end{cases} \tag{13}$$

The physical meanings of the variables in (13) are thoroughly explained in [34]. Variables prefixed with Δ represent the incremental values of their corresponding counterparts.

B. Temporary Frequency Support Capability Analysis

The temporary frequency support capability of a WT is associated with the strength of active power support, the length of support time and the amount of energy consumption, and such capability should be considered during the process of planning the temporary support trajectory. There are two methods to design the support trajectory of a WT, which are the P_{w}-ω_{w} curve [17] and the P_{w}-t curve [18], as shown in Fig. 7.

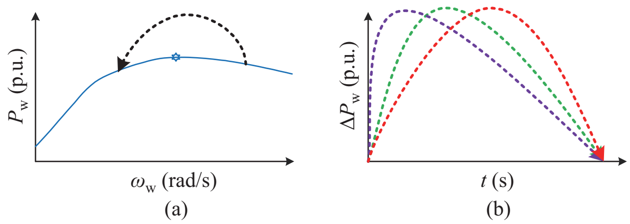

Fig. 7. Temporary frequency support trajectory in the coordinate system of (a) P_{w}-ω_{w}, (b) P_{w}-t.

Assuming that the P_{wm} is constant during the power support process, the support power is provided entirely by the rotor kinetic energy E_{wKE}, which can be expressed as:

$$E_{\mathrm{wKE}} = 0.5 J_{\mathrm{w}} (\omega_{\mathrm{w}}^2 - \omega_{\mathrm{min}}^2) \tag{14}$$

where J_{w} is the equivalent rotational inertia of the WT. The active power increment is constrained by the stored kinetic energy, deduced as:

$$\int_{t_0}^{t} \Delta P_{\mathrm{we}} \leq E_{\mathrm{wKE}} \tag{15}$$

Let the time step k correspond to the time t_0. The discrete form can be obtained as:

$$\sum_{k=1}^{n_k} \Delta P_{\mathrm{we}}(k) \leq E_{\mathrm{wKE}} \tag{16}$$

where n_k is the number of elements after discretization. Since the stored energy is predetermined, strong support in the early stage could lead to a weaker support later on. In addition, the maximum value and ramping rate of the active power are both constrained considering the mechanical load of the turbine. Therefore, the transient active power support capability of the WT is constrained in view of power and energy. Suppose an optimal support trajectory with energy and power constraints can be identified. In that case, it will be instructive for WPPs to improve the temporary frequency support capability and crucial for the frequency stability of the power system. Since the energy constraints are time-dependent, the P_{w}-t trajectory is more suitable for the OTFS strategy.

C. Predictive Model

Within the OTFS framework, it is essential to develop a predictive model to forecast the future behavior of the control variables. Fig. 8 illustrates the small-signal model for

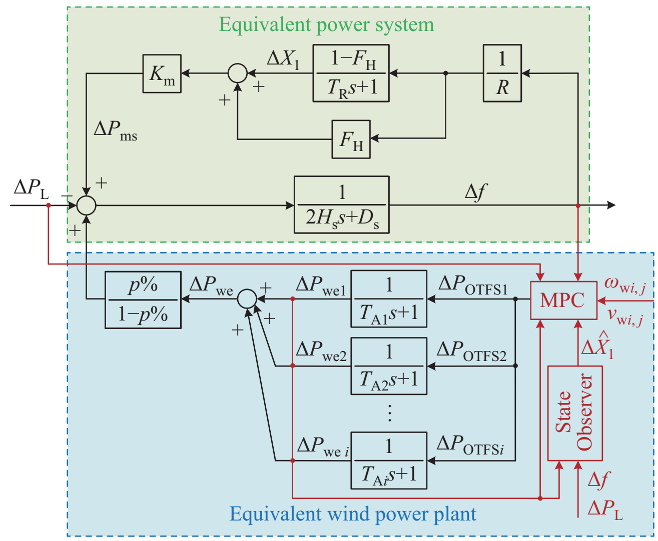

Fig. 8. Small-signal model for frequency response behavior of power system integrated with a WPP.

analyzing frequency response dynamics of the wind power integrated power system. To construct the equivalent power system, a low-order SFR model is employed. Given that the electromagnetic transient dynamics of a WT are significantly quicker than the electromechanical transients, the electromagnetic regulation processes of WTs and the converters can be neglected. Consequently, the active power control characteristics of wind generation are represented as an inertial element [45].

Although the purpose of the OTFS method is to tackle large power disturbances such as HVDC blocking, the resulting frequency variations are relatively small compared to the nominal value. Generally, the equivalent operation coefficient of the thermal generator remains unaffected during HVDC faults. Consequently, the nonlinearity associated with significant disturbances has limited influence on the behavior of this model. Additionally, the OTFS strategy is specifically developed for temporary frequency support, which results in the neglect of the SFC dynamics with a longer time scale.

According to Fig. 8, the state equations in matrix format can be obtained as:

$$\begin{cases} \dot{\boldsymbol{x}}(t) = \boldsymbol{A}\boldsymbol{x}(t) + \boldsymbol{B}\boldsymbol{u}(t) + \boldsymbol{E}d(t) \\ \boldsymbol{y}(t) = \boldsymbol{C}\boldsymbol{x}(t) \end{cases} \tag{17}$$

where n_{WT} is the number of WTs, $\boldsymbol{x} = [\Delta f, \Delta X_1, \Delta P_{\mathrm{we1}}, \Delta P_{\mathrm{we2}}, \cdots, \Delta P_{\mathrm{we}n\mathrm{WT}}, \Delta P_{\mathrm{OTFS1}}, \Delta P_{\mathrm{OTFS2}}, \cdots, \Delta P_{\mathrm{OTFS}n_{\mathrm{WT}}}]^{\mathrm{T}}$ is the state vector of the system, $\boldsymbol{u} = [u_1, u_2, \cdots, u_{n\mathrm{WT}}]^{\mathrm{T}}$ denotes the control vector of the system, $\boldsymbol{y} = [\Delta f, 0, \cdots, 0]^{\mathrm{T}}$ denotes the output of the system, $d = \Delta P_{\mathrm{L}}$ denotes the load perturbation of the system. It should be highlighted that the calculation time of the MPC algorithm cannot be neglected, and the time delay is equivalent to a first-order inertial element with a time constant T_τ. The input vector $\boldsymbol{u}$ is composed of the control variables optimized by the MPC algorithm. These control variables are then transformed through the inertial element to the $\Delta P_{\mathrm{OTFS1}}$ to

$\Delta P_{\mathrm{OTFS}n_{\mathrm{WT}}}$, which are the active power reference of OTFS for WTs and are considered as state variables.

As ΔX_1 cannot be directly measured by WPPs, it can be estimated using a state observer designed based on modern control theory principles. This method ensures that the system meets the required convergence rate and stability criteria. [34]. Then, the ΔX_1 is replaced by $\Delta\hat{X}_1$ in $\boldsymbol{x}$, and the $\boldsymbol{x} = [\Delta f, \Delta\hat{X}_1, \Delta P_{\mathrm{we}1}, \Delta P_{\mathrm{we}2}, \cdots, \Delta P_{\mathrm{we}n\mathrm{WT}}, \Delta P_{\mathrm{OTFS}1}, \Delta P_{\mathrm{OTFS}2}, \cdots, \Delta P_{\mathrm{OTFS}n_{\mathrm{WT}}}]^{\mathrm{T}}$. Matrices $\boldsymbol{A}$, $\boldsymbol{B}$, $\boldsymbol{C}$, and $\boldsymbol{E}$ are shown from (A1) to (A3) in Appendix A. By discretizing (17), the discrete state-space equation can be obtained

$$\begin{cases} \boldsymbol{x}(k+1) = \boldsymbol{G}\boldsymbol{x}(k) + \boldsymbol{H}\boldsymbol{u}(k) + \boldsymbol{I}d(k) \\ \boldsymbol{y}(k+1) = \boldsymbol{C}\boldsymbol{x}(k+1) \end{cases} \tag{18}$$

where $\boldsymbol{G} = \mathrm{e}^{\boldsymbol{A}t_{\mathrm{s}}}$, $\boldsymbol{H} = \int_0^{t_{\mathrm{s}}} \mathrm{e}^{\boldsymbol{A}t_{\mathrm{s}}}\boldsymbol{B}\mathrm{d}t$, $\boldsymbol{I} = \int_0^{t_{\mathrm{s}}} \mathrm{e}^{\boldsymbol{A}t_{\mathrm{s}}}\boldsymbol{E}\mathrm{d}t$, t_{s} denotes the sampling time, $\boldsymbol{x}$, d, and $\boldsymbol{y}$ represent the discrete forms of the corresponding variables in (17). Taking time point k as the reference, the system state variables from time point $k+1$ to $k+N_{\mathrm{p}}$ can be achieved according to (18), shown in

$$\begin{cases} \boldsymbol{X}(k+1) = \boldsymbol{G}_x\boldsymbol{x}(k) + \boldsymbol{H}_x\boldsymbol{U}(k) + \boldsymbol{I}_x\boldsymbol{D}(k) \\ \boldsymbol{Y}(k+1) = \boldsymbol{C}_y\boldsymbol{X}(k+1) \end{cases} \tag{19}$$

where $\boldsymbol{X}(k+1) = [\boldsymbol{x}(k+1), \boldsymbol{x}(k+2), \cdots, \boldsymbol{x}(k+N_{\mathrm{p}})]^{\mathrm{T}}$, $\boldsymbol{U}(k) = [\boldsymbol{u}(k), \boldsymbol{u}(k+1), \cdots, \boldsymbol{u}(k+N_{\mathrm{p}}-1)]^{\mathrm{T}}$, $\boldsymbol{D}(k) = [d(k), d(k+1), \cdots, d(k+N_{\mathrm{p}}-1)]^{\mathrm{T}}$, $\boldsymbol{Y}(k+1) = [\boldsymbol{y}(k+1), \boldsymbol{y}(k+2), \cdots, \boldsymbol{y}(k+N_{\mathrm{p}})]^{\mathrm{T}}$. Other matrices in (19) are shown from (A4) to (A6) in Appendix A, and N_{p} is the number of prediction/control horizon points.

D. Receding Horizon Optimization

After establishing the predictive model, a receding horizon optimization strategy needs to be explored. Predictive control draws from the concepts of optimal control by replacing static, global optimization with a receding horizon optimization framework over a finite time domain. The optimization algorithm is executed at each sampling time to derive active power support control signal sequence for future k steps. The first control signal of this sequence is then submitted to each WT. While global optimality cannot be theoretically guaranteed, in practice, real-time feedback-based optimization proves effective. This approach continuously accounts for inevitable model errors and environmental disturbances, such as wind speed fluctuations, and makes adaptive, timely adjustments.

The objective of the optimization is to minimize the magnitude of frequency drop and suppress the excessive actions of WTs. Here, the objective is described as minimizing the deviation and variation of grid frequency and active power reference of WTs in the receding period. The objective function can be expressed as:

$$\begin{aligned} \min\ J &= \boldsymbol{Y}(k+1)^T\boldsymbol{Q}_{\mathrm{Y}}\boldsymbol{Y}(k+1) \\ &+ \sum_{i=1}^{N_{\mathrm{p}}} \lambda_f |\Delta f(k+i) - \Delta f(k+i-1)| \\ &+ \boldsymbol{U}(k)^T\boldsymbol{R}_{\mathrm{U}}\boldsymbol{U}(k) + \sum_{i=1}^{N_{\mathrm{p}}} \lambda_u |\boldsymbol{u}(k+i) - \boldsymbol{u}(k+i-1)| \end{aligned} \tag{20}$$

where $\boldsymbol{Q}_{\mathrm{Y}}$ and $\boldsymbol{R}_{\mathrm{U}}$ are symmetric weighting matrices shown in (A7) in Appendix A, λ_f and λ_u are the weighting coefficients. Through the parameter debugging process, it was determined that setting λ_u to a mere 1/100$^{\mathrm{th}}$ of λ_f is sufficient for meeting the prescribed requirement, and these weighting coefficients do not require modification following system or disturbance changes.

The constraints are outlined below.

1) Incremental power of WTs:

$$\boldsymbol{u}_{\min} \leq \boldsymbol{u} \leq \boldsymbol{u}_{\max} \tag{21}$$

where $\boldsymbol{u}_{\max}$ and $\boldsymbol{u}_{\min}$ are the maximum and minimum incremental power of WTs in the receding period respectively.

2) Consumption of support energy of WTs:

$$\sum_{i=0}^{N_{\mathrm{p}}-1} \boldsymbol{u}(k+i) \leq [E_{\mathrm{wKE}1} \quad E_{\mathrm{wKE}2} \quad \cdots \quad E_{\mathrm{wKE}n_{\mathrm{WT}}}]^{\mathrm{T}} \tag{22}$$

where E_{wKE1} to E_{wKEi} are the kinetic energy stored in WT_1 to WT_i. Due to the requirement of computational efficiency for real-time control applications, the optimization problem should be linearized.

Through linearizing the absolute value item, the optimization problem can be reformulated as:

$$\begin{aligned} \min\ J = &\boldsymbol{Y}(k+1)^T\boldsymbol{Q}_{\mathrm{Y}}\boldsymbol{Y}(k+1) + \\ &\boldsymbol{U}(k)^T\boldsymbol{R}_{\mathrm{U}}\boldsymbol{U}(k) + \sum_{i=1}^{N_{\mathrm{p}}-1} (\lambda_f f_{\mathrm{z}i} + \lambda_u \boldsymbol{u}_{\mathrm{z}i}) \\ \text{s.t.}\ &\Delta f(k+i) - \Delta f(k+i-1) \leq f_{\mathrm{z}i} \\ &i = 1, 2, \cdots, N_{\mathrm{p}}-1 \\ &-\Delta f(k+i) + \Delta f(k+i-1) \leq f_{\mathrm{z}i} \\ &i = 1, 2, \cdots, N_{\mathrm{p}}-1 \\ &\boldsymbol{u}(k+i) - \boldsymbol{u}(k+i-1) \leq \boldsymbol{u}_{\mathrm{z}i} \\ &i = 1, 2, \cdots, N_{\mathrm{p}}-1 \\ &-\boldsymbol{u}(k+i) + \boldsymbol{u}(k+i-1) \leq \boldsymbol{u}_{\mathrm{z}i} \\ &i = 1, 2, \cdots, N_{\mathrm{p}}-1 \\ &\boldsymbol{u}_{\min}(k+i) \leq \boldsymbol{u}(k+i) \leq \boldsymbol{u}_{\max}(k+i) \\ &i = 0, 1, \cdots, N_{\mathrm{p}}-1 \\ &\sum_{i=0}^{N_{\mathrm{p}}-1} \boldsymbol{u}(k+i) \leq [E_{\mathrm{w}1} \quad E_{\mathrm{w}2} \quad \cdots \quad E_{\mathrm{w}n\mathrm{WT}}]^{\mathrm{T}} \end{aligned} \tag{23}$$

where $f_{\mathrm{z}i}$ and $\boldsymbol{u}_{\mathrm{z}i}$ are the intermediate variables required in the linearization.

The practical stability of MPC can be guaranteed by adjusting the weight matrices [46], [47]. Accordingly, the terminal cost is weighted to improve the convergence properties of the controller's output by increasing the last few diagonal elements of the weighting matrix $\boldsymbol{R}_{\mathrm{U}}$. The reason for not adding terminal weights to the weighting matrix $\boldsymbol{Q}_{\mathrm{Y}}$ is that the primary objective of this strategy is to minimize the depth of the frequency drop, rather than restoring the frequency to its nominal value. Increasing terminal weights in $\boldsymbol{Q}_{\mathrm{Y}}$ would alter this primary objective of the optimization.

At each sampling time, the optimization problem should be solved, and the optimal control variables should be updated and sent to the WT level. To make the strategy suitable for online control, the sampling interval should be longer than the calculation time of the optimization.

E. Feedback Correction

To mitigate inaccuracies in the predictive model, MPC incorporates feedback correction. The parameters of the predictive model are updated at 15-minute intervals using parameter estimation via the Levenberg-Marquardt method to ensure accuracy. Specifically, the parameters in matrices $\boldsymbol{A}$, $\boldsymbol{B}$, $\boldsymbol{C}$, and $\boldsymbol{E}$, along with their corresponding discrete counterparts, can be adjusted based on the data measured or estimated during the previous period.

V. Case Study

To validate the theoretical analysis and evaluate the effectiveness of the proposed OTFS scheme, a series of strategies are deployed within a 300 MW WPP, comprising 60 NREL 5 MW WTs. This WPP is integrated into a two-area system [48], as illustrated in Fig. 9. The WTs are spaced 600 meters apart. A total of 60 WTs are configured in 4 rows and 15 columns, aligned with the prevailing wind direction. These turbines are further categorized into 4 groups based on their respective rows, designated as WT1 to WT4. The SFR model in Fig. 8 is used in Section V-A, and the electromagnetic model is utilized in Section V-B.

The simulation platform, depicted in Fig. 10, comprises three main components: a personal computer (PC) equipped with an Intel i7-13620H CPU, a real-time simulator (RT-LAB OP5700), and an oscilloscope (Tektronix TDS 3054B). The 2-area power system and the WTs are loaded in the RT-LAB simulator. The MPC algorithm in the WPP controller is realized in the PC. The optimization problem is programmed based on the YALMIP and Matlab/Simulink to compute the control variables $\Delta P_{\mathrm{OTFS}i,j}$, which can be solved within 300 ms. These variables will be updated every 400 ms and sent to the RT-LAB through its I/O interface as control instructions for WTs. The prediction/control horizon consists of 75 steps, indicating that optimization accounts for scenarios anticipated over the next 30 seconds. This ensures that the prediction/control horizon encompasses the entire response process of the temporary frequency support, which typically stabilizes within 30 seconds considering the primary frequency control characteristics of SGs. Other key parameters of the simulation system are listed in Table I.

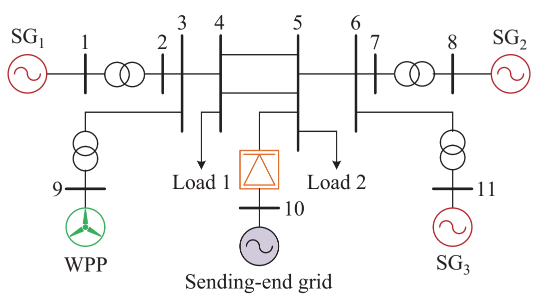

Fig. 9. The 2-area power system with a WPP integrated.

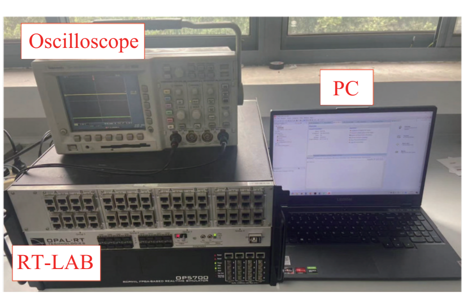

Fig. 10. RT-LAB platform.

TABLE I
Parameters of the Simulation System

SG Parameters	Values	WPP Parameters	Values
H_{s}, s	15	$p\%$	10%
D_{s}, p.u.	0.2	N_{p}	75
K_{m}	0.95	t_{s}, ms	400
F_{H}	0.3	T_{A}, s	0.2
R	-0.05	T_{τ}, s	0.4
T_{R}, s	8	t_{trig}, s	20
f_{dbd}, Hz	0.033	ω_{min}, p.u.	0.8
B, p.u./0.1 Hz	0.5	ω_{max}, p.u.	1.265

A. Analysis of Optimal Trajectories with Different Stored Kinetic Energy

To analyze the OTFS trajectory, the proposed strategy is implemented in the test system. Referring to the '9.19' Jinsu DC blocking incident in China, a DC blocking fault is simulated, resulting in a power loss of 0.06 pu. The system frequency curves and the support active power reference of WPP are shown in Fig. 11.

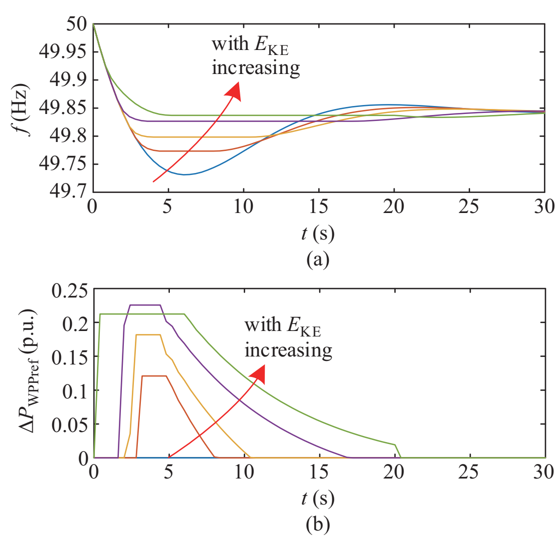

Fig. 11. Simulation of (a) system frequency, (b) active power support trajectories of WPP with E_{KE} increasing.

As illustrated in Fig. 11(a), the WPP with OTFS strategy can improve the FN effectively. The more energy utilized, the higher the FN. As shown in Fig. 11(b), in case of insufficient stored kinetic energy, WPP should reduce both the support active power magnitude and support time to ensure the support effect. Through an optimization of support active power magnitude and duration, it can target the FN for effective improvement. When the stored kinetic energy is sufficient, it is still not the case that the larger the support power the better the support effect. Since the WPP carries out temporary frequency support in contingency scenarios, the support power will eventually drop to zero, and the frequency value in the steady state is dependent on the primary frequency regulation. As can be seen from the green line in Fig. 11(a) and (b), the FN is almost the same as the stable value after the primary frequency regulation. Excessive support strength in the early stage will lead to the waste of kinetic energy and increase the difficulty of rotor speed recovery. Hence, the FN during the dynamic process is equivalent to the steady-state value, representing an optimal outcome that considers both energy consumption and FN. The trigger time for the TPPT strategy is set to 20 seconds after the disturbance occurs to ensure that the wind power plant exits frequency support only after the convergence of $\Delta P_{\mathrm{WPPref}}$, thereby preventing a SFD. When sufficient kinetic energy is stored, as illustrated by the green line in Fig. 11, the active power support from the WPP will decrease to zero at $t = 20$ s.

B. Different Strategies Analysis

The performance of the proposed strategy within the whole frequency support duration is evaluated. In this section, the DC fault is the same as the case in Section V-A. The frequency response characteristics with OTFS and other traditional strategies are analyzed with different wind speeds. To focus on the analysis of the temporary frequency support stage, results for only the first minute after the fault occurrence are presented in Section V-B1), and the complete process including the recovery of the WTs' rotor speed is analyzed in Section V-B2). The wind fields are generated in the SimWindFarm toolbox.

1) Strategies Comparison with Low Wind Speed

Five existing strategies, MPC-based SIC (MPC-SIC) [22], power reserve control (PRC) [36], RoCoF-Droop-based coordinated control (RCC) [14], traditional temporary frequency support (TTFS) [28] and MPPT control, are employed. The mean speed of the upstream wind is 8 m/s, and the turbulence intensity is 0.02, as depicted in Fig. 12(a).

The system frequency, active power reference of WPP, active power output, and rotor speed of WTs with different frequency support strategies are shown in Fig. 12. It can be seen from Fig. 12(b) and Table II that the FN with the OTFS method is higher than that with other traditional methods. The WTs with PRC will provide primary frequency control in the stable operation region, and the SFD is prevented accordingly. Yet, the WTs with RCC strategy will provide virtual inertia response and primary frequency control during the frequency support period, which will let the rotor speed drop to the temporary region, resulting in the SFD. For the MPC-SIC, since it will lead to a considerable disturbance to the power system with its withdrawal from the frequency support, the SFD can be more severe. The TTFS strategy improves the FN by designing control algorithms that enable the active power output of WPP to counteract the dynamic frequency fluctuations caused by the delay in the primary frequency response of SGs. However, it does not account for variations in wind speed in its parameter design process. We adjust the parameters based on wind conditions, aiming to maximize the frequency regulation gain coefficients while ensuring the safe rotational speed of WTs. Despite these adjustments, as shown in Table II, the FN achieved by the TTFS strategy remains inferior to that provided by the OTFS strategy. From Fig. 12(b) and (c), it can be obtained that the power reference of OTFS is smoother at the end of the temporary frequency support, and accordingly, the SFD is avoided. Besides, the support active power reference of OTFS is not the highest at the initial stage, indicating that OTFS achieves the improvement of the FN with small active power variations.

TABLE II
FREQUENCY NADIR WITH DIFFERENT STRATEGIES

Strategy	OTFS	PRC	RCC	MPC-SIC	TTFS	MPPT
FN (Hz)	49.82	49.80	49.80	49.80	49.81	49.73

The active power output of each WT with different frequency support strategies is shown in Fig. 12(d1) to (d5). As illustrated in Fig. 12(e), the WTs with the OTFS strategy stabilized near the lower speed limit after the temporary frequency support, taking full utilization of energy within constraints. Moreover, the traditional methods need to recover the rotor speed to the regular operation after the frequency support (in Fig. 12(e3) to (e5)), while OTFS allows WTs to maintain the current speed after the temporary frequency support and wait for the SFC of the system.

2) Strategies Comparison with High Wind Speed

To test the performance of the proposed strategy with more stored kinetic energy, the mean speed of the upstream wind is increased to 10 m/s, as shown in Fig. 13(a). The simulation duration is increased to 3 minutes to show the whole process from frequency drop to recovery.

The system frequency, active power reference of WPP, active power output of WTs, and rotor speed of WTs with different frequency support strategies are shown in Fig. 13. In Fig. 13(b), the MPC-based OTFS strategy is initiated at $t =$ 10 s and concludes at $t = 30$ s when the TPPT strategy is activated. The TPPT strategy persists for 45 s and terminates at $t = 75$ s, approximately 5 s after the initiation of the SFC. Then, the rotor speed of the WTs gradually returns to the steady-state operational point, following the power-rotor speed trajectory designed in Section III-D. As a result of SFC, the system frequency increases, but it will not accurately return to the nominal value due to the presence of the SFC dead band.

Figure 13(b) illustrates that the proposed OTFS strategy demonstrates a higher FN compared to traditional methods. It is worth noting that the active power reference of the WPP utilizing the OTFS method is not the highest. This observation suggests that OTFS effectively enhances the FN by strategically utilizing kinetic energy. The TTFS strategy employs a fixed support mode and lacks the flexibility to adjust based on the operational states of individual WTs. The corresponding FN with the TTFS strategy is 49.83 Hz in this scenario, as presented in Table III, which did not perform as effectively as the OTFS strategy in terms of frequency

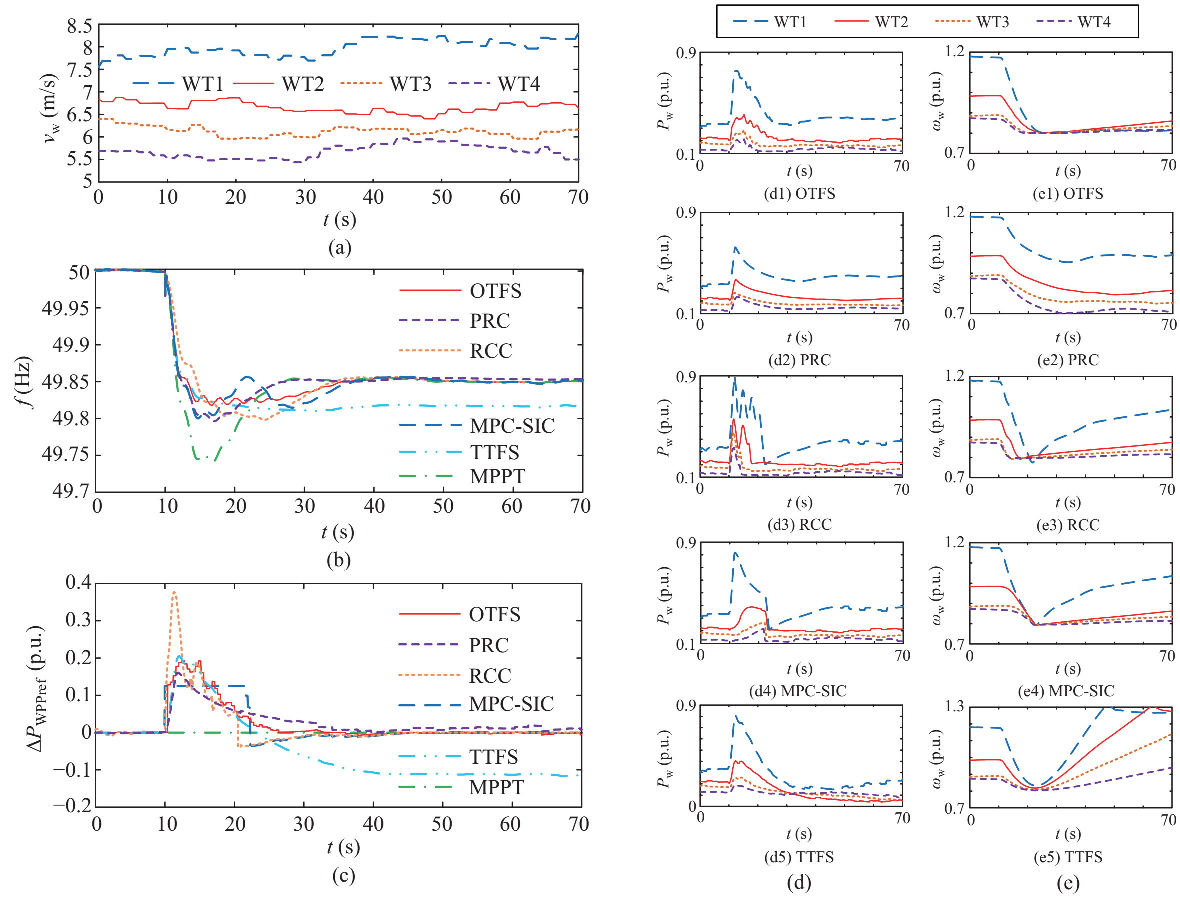

Fig. 12. Simulation of different strategies with low wind speed. (a) Wind speed. (b) System frequency. (c) Active power support trajectory. (d) Active power output. (e) Rotor speed.

TABLE III
FREQUENCY NADIR WITH DIFFERENT STRATEGIES

Strategy	OTFS	PRC	RCC	MPC-SIC	TTFS	MPPT
FN (Hz)	49.84	49.80	49.79	49.79	49.83	49.73

support. The control parameters for TTFS used in this instance are determined through extensive tuning. Any further increase in the control coefficients of TTFS could lead to excessive reductions in WTs' rotor speeds, forcing an early withdrawal from frequency regulation and resulting in a SFD, thereby further lowering the FN. A comparison of Tables II and III reveals that after an increase in wind speed, the FN is actually lower with the RCC and MPC-SIC strategies. This is attributed to the higher rotor speeds at which WTs, following the MPPT curve, experience larger power drops during speed recovery, implying a greater secondary disturbance to the system.

The active power output and rotor speed of each WT with different frequency support strategies are shown in Fig. 13(d) and (e) respectively. Fig. 13(e1) illustrates that the recovery of rotor speed for WT1, WT3, and WT4 initiates at $t = 75$ s, whereas WT2 starts recovering its speed at approximately $t = 40$ s. This distinction arises from the fact that WT2 did not enter the temporary region on the left side of the MPPT curve and, consequently, did not activate the TPPT strategy.

3) Strategies Comparison with High Wind Speed and High Turbulence

To test the effectiveness of the proposed strategy under more significant wind speed fluctuations, a wind field with an average upstream speed of 10 m/s and a turbulence intensity of 0.1 is generated, as shown in Fig. 14(a), which more closely resembles the real-world wind fluctuations [49]. Other simulation parameters remain the same as those set in Section V-B2).

The system frequency, active power reference of WPP, active power output of WTs, and rotor speed of WTs with different frequency support strategies are shown in Fig. 14. In comparison to the scenario described in Section V-B2), a significant deviation in the present case is the early termination of frequency regulation by the WPP employing the TTFS strategy, specifically due to a reduction in the rotor speed of WT_1 to its lower limit. This results in a notable SFD to 49.80 Hz around $t = 50$ s, as illustrated in Fig. 14(b) and Table IV. In the previous cases, the control parameters of the TTFS strategy were adjusted to accommodate varying wind conditions, often necessitating multiple iterations to optimize the parameters. In this scenario, the mean value of the wind speed, the initial stored kinetic energy of each WT, along with the control parameters of the TTFS strategy are consistent with those in Section V-B2. The only difference is the increased turbulence intensity. This underscores the inability of the TTFS strategy to dynamically adjust the support strength based

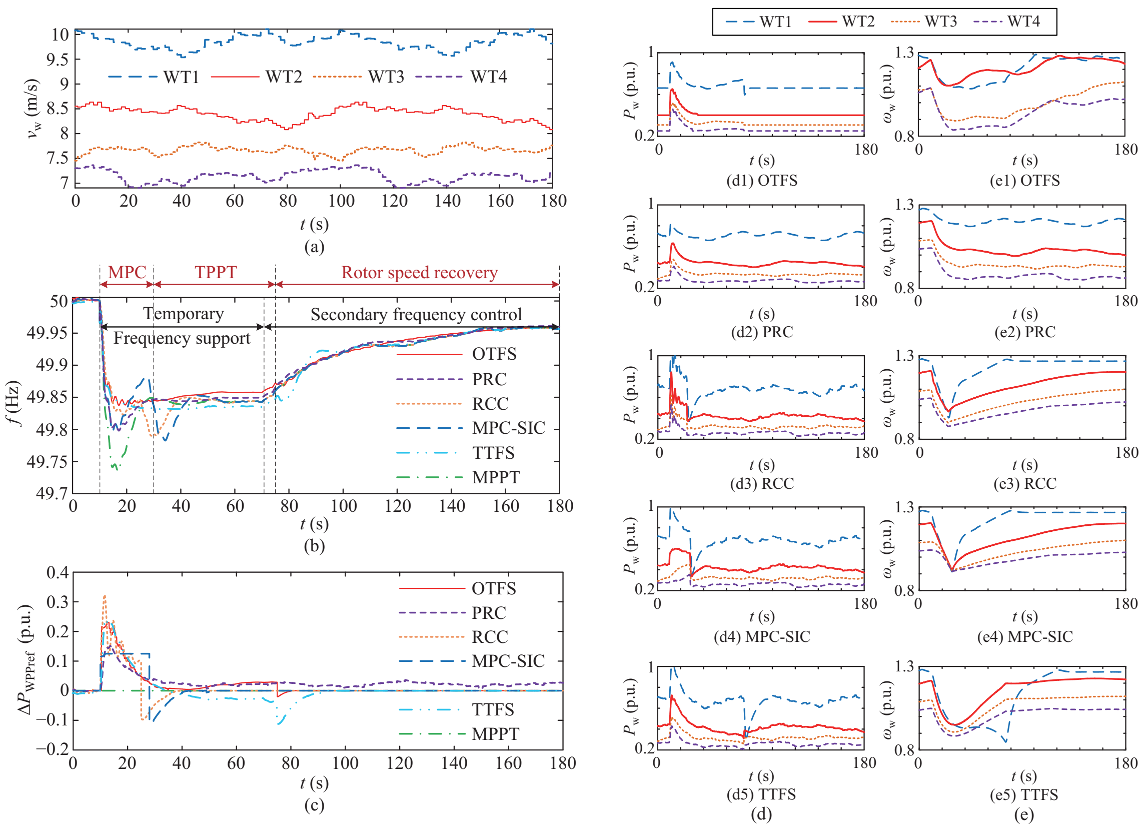

Fig. 13. Simulation of different strategies with high wind speed. (a) Wind speed. (b) System frequency. (c) Active power support trajectory. (d) Active power output. (e) Rotor speed.

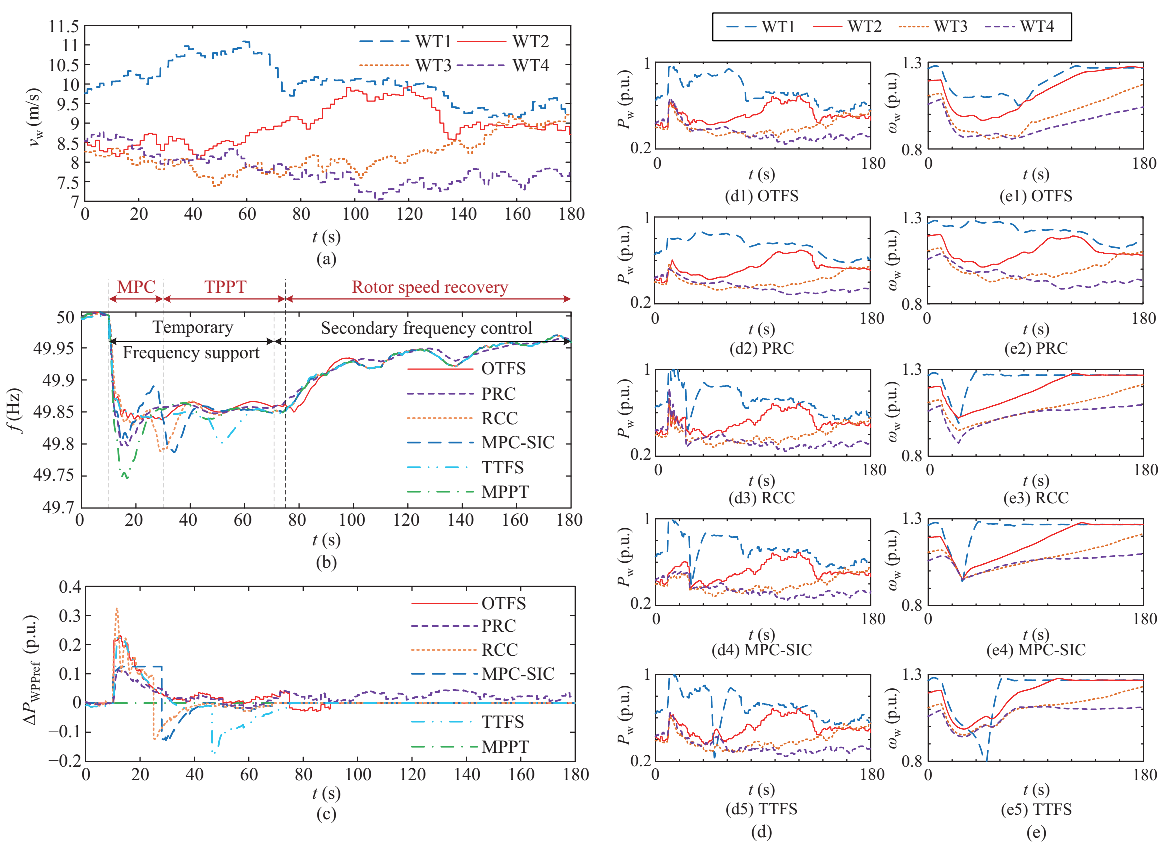

Fig. 14. Simulation of different strategies with high wind speed and high turbulence intensity. (a) Wind speed. (b) System frequency. (c) Active power support trajectory. (d) Active power output. (e) Rotor speed.

TABLE IV
FREQUENCY NADIR WITH DIFFERENT STRATEGIES

Strategy	OTFS	PRC	RCC	MPC-SIC	TTFS	MPPT
FN (Hz)	49.84	49.80	49.79	49.79	49.80	49.73

on fluctuations in wind speed and the WT's stored kinetic energy. This scenario validates the effectiveness and robustness of employing the receding horizon optimization approach, which not only seeks an optimal solution at the moment of disturbance occurrence but also dynamically adjusts the control instructions during the response process based on the operating conditions of WTs.

VI. CONCLUSION

In this paper, an OTFS strategy is proposed for the WPP to improve the FN of the power system. The strategy incorporates the TPPT strategy, not only enhancing their frequency support capabilities but also mitigating the SFD. The power support trajectory of each WT is dynamically optimized considering the specific support capability of WTs and the overarching needs of the power system, thereby achieving the optimal FN with efficient energy utilization.

Case studies confirm the strategy's suitability for real-time control and demonstrate its effectiveness and superiority over traditional methods. The findings suggest that initiating support actions proximal to the occurrence frequency nadir, particularly when kinetic energy reserves are low, proves more effective than earlier and stronger active power interventions. When the stored kinetic energy is sufficient, the OTFS strategy enables the FN to closely approximate the stable value following the primary frequency regulation.

APPENDIX A

$$\boldsymbol{A}=\begin{bmatrix} \frac{K_{\mathrm{m}}F_{\mathrm{H}}-D_{\mathrm{s}}R}{2H_{\mathrm{s}}R} & \frac{K_{\mathrm{m}}}{2H_{\mathrm{s}}} & \frac{p\%}{2H_{\mathrm{s}}(1-p\%)} & \cdots & \frac{p\%}{2H_{\mathrm{s}}(1-p\%)} & 0 & \cdots & 0 \\ \frac{1-F_{\mathrm{H}}}{T_{\mathrm{R}}R} & -\frac{1}{T_{\mathrm{R}}} & 0 & \cdots & 0 & 0 & \cdots & 0 \\ 0 & 0 & -\frac{1}{T_{\mathrm{A1}}} & & 0 & \frac{1}{T_{\mathrm{A1}}} & & 0 \\ \vdots & \vdots & & \ddots & & & \ddots & \\ 0 & 0 & 0 & & -\frac{1}{T_{\mathrm{A}n_{\mathrm{WT}}}} & 0 & & \frac{1}{T_{\mathrm{A}n_{\mathrm{WT}}}} \\ 0 & 0 & 0 & & 0 & -\frac{1}{T_\tau} & & 0 \\ \vdots & \vdots & & \ddots & & & \ddots & \\ 0 & 0 & 0 & & 0 & 0 & & -\frac{1}{T_\tau} \end{bmatrix} \tag{A1}$$

$$\boldsymbol{B}=\begin{bmatrix} 0 & 0 & 0 & & 0 & \frac{1}{T_\tau} & & 0 \\ \vdots & \vdots & & \ddots & & & \ddots & \\ 0 & 0 & 0 & & 0 & 0 & & \frac{1}{T_\tau} \end{bmatrix}^{\mathrm{T}}$$

$$\boldsymbol{C}=\begin{bmatrix} 1 & 0 & 0 & \cdots & 0 \\ 0 & 0 & 0 & \cdots & 0 \\ \vdots & \vdots & \vdots & & \vdots \\ 0 & 0 & 0 & \cdots & 0 \end{bmatrix} \tag{A2}$$

$$\boldsymbol{E}=\begin{bmatrix} -\frac{1}{2H_{\mathrm{s}}} & 0 & 0 & \cdots & 0 \end{bmatrix}^{\mathrm{T}} \tag{A3}$$

$$\boldsymbol{G}_x=[\boldsymbol{G} \;\; \boldsymbol{G}^2 \;\; \cdots \;\; \boldsymbol{G}^{N_{\mathrm{P}}}]^{\mathrm{T}} \tag{A4}$$

$$\boldsymbol{H}_x=\begin{bmatrix} \boldsymbol{H} & 0 & \cdots & 0 \\ \boldsymbol{GH} & \boldsymbol{H} & \cdots & 0 \\ \boldsymbol{G}^2\boldsymbol{H} & \boldsymbol{GH} & \cdots & 0 \\ \vdots & \vdots & & \vdots \\ \boldsymbol{G}^{N_{\mathrm{P}}-1}\boldsymbol{H} & \boldsymbol{G}^{N_{\mathrm{P}}-2}\boldsymbol{H} & \cdots & \boldsymbol{H} \end{bmatrix}$$

$$\boldsymbol{I}_x=\begin{bmatrix} \boldsymbol{I} & 0 & \cdots & 0 \\ \boldsymbol{GI} & \boldsymbol{I} & \cdots & 0 \\ \boldsymbol{G}^2\boldsymbol{I} & \boldsymbol{GI} & \cdots & 0 \\ \vdots & \vdots & & \vdots \\ \boldsymbol{G}^{N_{\mathrm{P}}-1}\boldsymbol{I} & \boldsymbol{G}^{N_{\mathrm{P}}-2}\boldsymbol{I} & \cdots & \boldsymbol{I} \end{bmatrix} \tag{A5}$$

$$\boldsymbol{C}_y=[\boldsymbol{C} \;\; \boldsymbol{C} \;\; \cdots \;\; \boldsymbol{C}]^{\mathrm{T}} \tag{A6}$$

$$\boldsymbol{Q}_{\mathrm{Y}}=\begin{bmatrix} \boldsymbol{Q}_1 & & 0 \\ & \ddots & \\ 0 & & \boldsymbol{Q}_{N_{\mathrm{P}}} \end{bmatrix},\; \boldsymbol{R}_{\mathrm{U}}=\begin{bmatrix} \boldsymbol{R}_1 & & 0 \\ & \ddots & \\ 0 & & \boldsymbol{R}_{N_{\mathrm{P}}} \end{bmatrix} \tag{A7}$$

REFERENCES

[1] X. Ding, W. Lin, J. Xu, Y. Z. Sun, L. Z. Yao, and B. L. Mao, "Coordinated frequency control for isolated power systems with high penetration of DFIG-based wind power," *CSEE Journal of Power and Energy Systems*, vol. 10, no. 4, pp. 1399–1414, Jul. 2024, doi: 10.17775/CSEEJPES.2021.08320.

[2] L. Li, D. H. Zhu, X. D. Zou, J. B. Hu, Y. Kang, and J. M. Guerrero, "Review of frequency regulation requirements for wind power plants in international grid codes," *Renewable and Sustainable Energy Reviews*, vol. 187, pp. 113731, Nov. 2023.

[3] Y. H. Yao, W. Yao, Y. X. Xiong, S. Q. Lin, H. Y. Zhou, J. Y. Wen, S. J. Cheng, "Distributed adaptive leaderless consensus control of wind farm for fast frequency support," *IEEE Transactions on Industrial Electronics*, vol. 71, no. 10, pp. 12255–12266, Oct. 2024, doi: 10.1109/TIE.2023.3347857.

[4] B. Liu, J. B. Zhao, Q. Huang, F. Milano, Y. C. Zhang, and W. H. Hu, "Nonlinear virtual inertia control of WTGs for enhancing primary frequency response and suppressing drivetrain torsional oscillations," *IEEE Transactions on Power Systems*, vol. 36, no. 5, pp. 4102–4113, Sep. 2021.

[5] Y. D. Ye, Y. Qiao, and Z. X. Lu, "Revolution of frequency regulation in the converter-dominated power system," *Renewable and Sustainable Energy Reviews*, vol. 111, pp. 145–156, Sep. 2019.

[6] H. Zhu et al., "Energy storage in high variable renewable energy penetration power systems: Technologies and applications," in *CSEE Journal of Power and Energy Systems*, vol. 9, no. 6, pp. 2099–2108, Nov. 2023, doi: 10.17775/CSEEJPES.2020.00090.

[7] Z. W. Li, X. L. Wu, K. Q. Zhuang, L. Wang, Y. C. Miao, and B. J. Li, "Analysis and reflection on frequency characteristics of east China grid after bipolar locking of '9· 19' Jinping-Sunan DC transmission line," *Automation of Electric Power Systems*, vol. 41, no. 7, pp. 149–155, Apr. 2017.

[8] (2019, Sep.). Technical report on the events of 9 August 2019. [Online]. Available: https://www.nationalgrideso.com/document/152346/download

[9] National Grid Electricity System Operator Limited. (2023, Jan.). The grid code. [Online]. Available: https://www.nationalgrideso.com/document/162271/download

[10] E. Nycander and L. Söder, "Review of European grid codes for wind farms and their implications for wind power curtailments," *17th International Wind Integration Workshop Stockholm*, 2018.

[11] *Technical Specification for Connecting Wind Farm to Power System—Part 1: On Shore Wind Power*, GB/T 19963.1–2021, 2021.

[12] G. Lalor, A. Mullane, and M. O'Malley, "Frequency control and wind turbine technologies," *IEEE Transactions on Power Systems*, vol. 20, no. 4, pp. 1905–1913, Nov. 2005.

[13] J. Morren, S. W. H. de Haan, W. L. Kling, and J. A. Ferreira, "Wind turbines emulating inertia and supporting primary frequency control," *IEEE Transactions on Power Systems*, vol. 21, no. 1, pp. 433–434, Feb. 2006.

[14] Z. G. Wang and W. C. Wu, "Coordinated control method for DFIG-based wind farm to provide primary frequency regulation service," *IEEE Transactions on Power Systems*, vol. 33, no. 3, pp. 2644–2659, May 2018.

[15] J. Lee, G. Jang, E. Muljadi, F. Blaabjerg, Z. Chen, and Y. C. Kang, "Stable short-term frequency support using adaptive gains for a DFIG-based wind power plant," *IEEE Transactions on Energy Conversion* , vol. 31, no. 3, pp. 1068–1079, Sep. 2016.

[16] L. A. G. Gomez, L. F. N. Lourenço, A. P. Grilo, M. B. C. Salles, L. Meegahapola, and A. J. Sguarezi Filho, "Primary frequency response of microgrid using doubly fed induction generator with finite control set model predictive control plus droop control and storage system," *IEEE Access*, vol. 8, pp. 189298–189312, Oct. 2020.

[17] M. Kheshti, S. Y. Lin, X. W. Zhao, L. Ding, M. H. Yin, and V. Terzija, "Gaussian distribution-based inertial control of wind turbine generators for fast frequency response in low inertia systems," *IEEE Transactions on Sustainable Energy*, vol. 13, no. 3, pp. 1641–1653, Jul. 2022.

[18] D. J. Yang, J. Kim, Y. C. Kang, E. Muljadi, N. Zhang, J. Hong, S. H. Song, and T. Y. Zheng, "Temporary frequency support of a DFIG for high wind power penetration," *IEEE Transactions on Power Systems*, vol. 33, no. 3, pp. 3428–3437, May 2018.

[19] N. R. Ullah, T. Thiringer, and D. Karlsson, "Temporary primary frequency control support by variable speed wind turbines—potential and applications," *IEEE Transactions on Power Systems*, vol. 23, no. 2, pp. 601–612, May 2008.

[20] M. Kang, K. Kim, E. Muljadi, J. W. Park, and Y. C. Kang, "Frequency control support of a doubly-fed induction generator based on the torque limit," *IEEE Transactions on Power Systems*, vol. 31, no. 6, pp. 4575–4583, Nov. 2016.

[21] M. Kheshti, L. Ding, W. Y. Bao, M. H. Yin, Q. W. Wu, and V. Terzija, "Toward intelligent inertial frequency participation of wind farms for the grid frequency control," *IEEE Transactions on Industrial Informatics*, vol. 16, no. 11, pp. 6772–6786, Nov. 2020.

[22] W. Y. Bao, Q. W. Wu, L. Ding, S. Huang, and V. Terzija, "A hierarchical inertial control scheme for multiple wind farms with BESSs based on ADMM," *IEEE Transactions on Sustainable Energy*, vol. 12, no. 2, pp. 751–760, Apr. 2021.

[23] Y. N. Zhou, D. H. Zhu, X. D. Zou, C. Y. He, J. B. Hu, and Y. Kang, "Adaptive temporary frequency support for DFIG-based wind turbines," *IEEE Transactions on Energy Conversion*, vol. 38, no. 3, pp. 1937–1949, Sep. 2023.

[24] K. C. Liu, Y. B. Qu, H. M. Kim, and H. H. Song, "Avoiding frequency second dip in power unreserved control during wind power rotational speed recovery," *IEEE Transactions on Power Systems*, vol. 33, no. 3, pp. 3097–3106, May 2018.

[25] Y. Cheng, R. Azizipanah-Abarghooee, S. Azizi, L. Ding, and V. Terzija, "Smart frequency control in low inertia energy systems based on frequency response techniques: a review," *Applied Energy*, vol. 279, pp. 115798, Dec. 2020.

[26] Y. Wang, J. H. Meng, X. Y. Zhang, and L. Xu, "Control of PMSG-based wind turbines for system inertial response and power oscillation damping," *IEEE Transactions on Sustainable Energy*, vol. 6, no. 2, pp. 565–574, Apr. 2015.

[27] X. L. Zhao, Z. Y. Lin, B. Fu, and S. L. Gong, "Research on frequency control method for micro-grid with a hybrid approach of FFR-OPPT and pitch angle of wind turbine," *International Journal of Electrical Power & Energy Systems*, vol. 127, pp. 106670, May 2021.

[28] M. Sun, Y. Sun, L. Chen, Z. B. Zou, Y. Min, R. K. Liu, F. Xu, and Y. Y. Wu, "Novel temporary frequency support control strategy of wind turbine generator considering coordination with synchronous generator," *IEEE Transactions on Sustainable Energy*, vol. 13, no. 2, pp. 1011–1020, Apr. 2022.

[29] G. Zhang, F. Zhang, L. Ding, K. Meng, and Z. Y. Dong, "Wind farm level coordination for optimal inertial control with a second-order cone predictive model," *IEEE Transactions on Sustainable Energy*, vol. 12, no. 4, pp. 2353–2366, Oct. 2021.

[30] H. Q. Liu, M. X. Li, L. Liu, and J. Q. Shi, "Frequency trajectory planning-based transient frequency regulation strategy for wind turbine systems," *IEEE Journal of Emerging and Selected Topics in Power Electronics*, vol. 10, no. 4, pp. 3987–4000, Aug. 2022.

[31] Y. C. Liang, X. W. Zhao, and L. Sun, "A multiagent reinforcement learning approach for wind farm frequency control," *IEEE Transactions on Industrial Informatics*, vol. 19, no. 2, pp. 1725–1734, Feb. 2023.

[32] Z. Z. Guo and W. C. Wu, "Data-driven model predictive control method for wind farms to provide frequency support," *IEEE Transactions on Energy Conversion*, vol. 37, no. 2, pp. 1304–1313, Jun. 2022.

[33] J. X. Ouyang, M. Y. Pang, M. Y. Li, D. Zheng, T. Tang, and W. Wang, "Frequency control method based on the dynamic deloading of DFIGs for power systems with high-proportion wind energy," *International Journal of Electrical Power & Energy Systems*, vol. 128, pp. 106764, Jun. 2021.

[34] Z. Y. Hu, B. T. Gao, and R. Z. Sun, "An active primary frequency regulation strategy for grid integrated wind farms based on model predictive control," *Sustainable Energy, Grids and Networks*, vol. 32, pp. 100955, Dec. 2022.

[35] X. Lyu, Y. W. Jia, and Z. Xu, "A novel control strategy for wind farm active power regulation considering wake interaction," *IEEE Transactions on Sustainable Energy*, vol. 11, no. 2, pp. 618–628, Apr. 2020.

[36] S. Q. Wang and K. Tomsovic, "A novel active power control framework for wind turbine generators to improve frequency response," *IEEE Transactions on Power Systems*, vol. 33, no. 6, pp. 6579–6589, Nov. 2018.

[37] Y. J. Li, Z. Xu, J. L. Zhang, H. M. Yang, and K. P. Wong, "Variable utilization-level scheme for load-sharing control of wind farm," *IEEE Transactions on Energy Conversion*, vol. 33, no. 2, pp. 856–868, Jun. 2018.

[38] H. R. Zhao, Q. W. Wu, S. J. Huang, M. Shahidehpour, Q. L. Guo, and H. B. Sun, "Fatigue load sensitivity-based optimal active power dispatch for wind farms," *IEEE Transactions on Sustainable Energy*, vol. 8, no. 3, pp. 1247–1259, Jul. 2017.

[39] J. H. Chow, "Enabling inverter-based resource stability control in power systems with high renewable penetration," in *CSEE Journal of Power and Energy Systems*, vol. 9, no. 3, pp. 1248–1250, May 2023, doi: 10.17775/CSEEJPES.2022.08000.

[40] X. S. Tang, M. H. Yin, C. Shen, Y. Xu, Z. Y. Dong, and Y. Zou, "Active power control of wind turbine generators via coordinated rotor speed and pitch angle regulation," *IEEE Transactions on Sustainable Energy*, vol. 10, no. 2, pp. 822–832, Apr. 2019.

[41] X. Fang, H. Y. Yuan, and J. Tan, "Secondary frequency regulation from variable generation through uncertainty decomposition: an economic and reliability perspective," *IEEE Transactions on Sustainable Energy*, vol. 12, no. 4, pp. 2019–2030, Oct. 2021.

[42] R. Patel, C. J. Li, L. Meegahapola, B. McGrath, and X. H. Yu, "Enhancing optimal automatic generation control in a multi-area power system with diverse energy resources," *IEEE Transactions on Power Systems*, vol. 34, no. 5, pp. 3465–3475, Sep. 2019.

[43] A. K. Bejestani, A. Annaswamy, and T. Samad, "A hierarchical transactive control architecture for renewables integration in smart grids: analytical modeling and stability," *IEEE Transactions on Smart Grid*, vol. 5, no. 4, pp. 2054–2065, Jul. 2014.

[44] P. M. Anderson and M. Mirheydar, "A low-order system frequency response model," *IEEE Transactions on Power Systems*, vol. 5, no. 3, pp. 720–729, Aug. 1990.

[45] Z. W. Lin, Z. Y. Chen, C. Z. Qu, Y. F. Guo, J. Z. Liu, and Q. W. Wu, "A hierarchical clustering-based optimization strategy for active power dispatch of large-scale wind farm," *International Journal of Electrical Power & Energy Systems*, vol. 121, pp. 106155, Oct. 2020.

[46] D. Limon, T. Alamo, F. Salas, and E. F. Camacho, "On the stability of constrained MPC without terminal constraint," *IEEE Transactions on Automatic Control*, vol. 51, no. 5, pp. 832–836, May 2006.

[47] V. Yaramasu and B. Wu, *Model Predictive Control of Wind Energy Conversion Systems*, Piscataqay: John Wiley & Sons, 2016.

[48] P. S. Kundur, *Power System Stability and Control*, New York: McGraw-Hill, 1994.

[49] G. R. Ren, J. F. Liu, J. Wan, F. Li, Y. F. Guo, and D. R. Yu, "The analysis of turbulence intensity based on wind speed data in onshore wind farms," *Renewable Energy*, vol. 123, pp. 756–766, Aug. 2018.

Zhengyang Hu received the B.E. degree in Electrical Engineering and Automation from China University of Mining and Technology, Xuzhou, China in 2016, and the Ph.D. degree in Electrical Engineering from Southeast University, Nanjing, China in 2023. He is currently working as a Postdoctoral Fellow with The Hong Kong Polytechnic University. His research interests include renewable energy grid-integration, power system inertia and frequency control, and power system resilience.

Bingtuan Gao received the B.E degree in Electrical Engineering and Automation, the M.E. degree in Control Theory and Control Engineering, and the Ph.D. degree in Power Electronics and Electrical Drive from the Harbin Institute of Technology, Harbin, China, in 2002, 2004, and 2007, respectively. From 2008 to 2010, he held a postdoctoral position with the Department of Electrical and Computer Engineering, Michigan State University, East Lansing, USA. He is currently a Professor with the School of Electrical Engineering, Southeast University, Nanjing, China. His research interests include robotics and its application in smart grid, optimization and control of power system integrated with renewable energy, demand side management, distributed energy system.

Zhao Xu received the B.Eng. degree from Zhejiang University, Hangzhou, China, in 1996, the M.Eng. degree from the National University of Singapore, Singapore, in 2002, and the Ph.D. degree from The University of Queensland, Brisbane, QLD, Australia, in 2006, all in Electrical Engineering. From 2006 to 2010, he was an Assistant and then an Associate Professor with the Department of Electrical Engineering, Technical University of Denmark, Kongens Lyngby, Denmark. Since 2010, he has been with The Hong Kong Polytechnic University, Hong Kong, China, where he is currently a Professor with the Department of Electrical Engineering and the Leader of Smart Grid Research Area. He is also a foreign Associate Staff of the Centre for Electric Technology, Technical University of Denmark. His research interests include smart grid, renewable energy, and applications of AI and big data analytics. He has extensive research project experiences involving collaborations with academia, industrial, and business sectors. Prof. Xu was the recipient of several awards for research excellence, including 2017 State Award in Nature Science from MOE, China. He is currently the Chairman of the IEEE Hong Kong Joint Chapter of PES/IELS/IAS/PELS. He has served/is serving as an editor for a number of IEEE Transactions and IET journals.

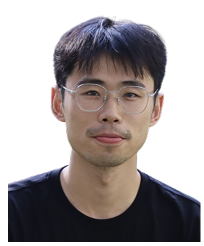

Sufan Jiang received the B.S.E.E., M.S.E.E., and Ph.D. degrees from Southeast University, Nanjing, China, in 2014, 2017, and 2022, respectively. Currently, he is a research scientist at the University of Tennessee, Knoxville (UTK), TN, USA. His research interests include resilience, flexibility, and energy policy in power systems.